Design, Operation, and Calibration of a Shipboard Fast-Rotating Shadowband Spectral Radiometer

R. MICHAEL REYNOLDS, MARK A. MILLER, AND MARY J. BARTHOLOMEW

Brookhaven National Laboratory, Upton, New York

(Manuscript received 23 November 1999, in final form 5 June 2000)

ABSTRACT

This paper describes the design, calibration, and deployment of a fast-rotating shadowband radiometer (FRSR) that accurately decomposes downward shortwave (solar) irradiance into direct-beam and diffuse components from a moving platform, such as a ship on the ocean. The FRSR has seven channels, one broad-band silicone detector, and six 10-nm-wide channels at 415, 500, 610, 660, 860, and 940 nm. The shadowband technique produces estimates of the direct-beam normal irradiance, the diffuse irradiance (sky component), and the total irradiance. The direct-beam normal irradiances produce time series of aerosol optical thickness. A proven ability to derive meaningful at-sea estimates of aerosol optical depth from an economical, automated, and reliable instrument opens the way to a distributed network of such measurements from volunteer observing ships in all areas of the World Ocean. The processing algorithms are key to the instrument's ability to derive direct-normal beam irradiance without gimbals and a gyro-stabilized table. At-sea Langley plots were produced during the Aerosols99 cruise of the R/V *Ronald H. Brown* from Norfolk, Virginia, to Cape Town, South Africa. A Langley calibration of the instrument at the Mauna Loa Observatory confirmed prior calibrations and demonstrated that the calibration was stable over the duration of the cruise. The standard deviation in all plots was of the order 2% for all channels.

1. Introduction

Aerosols over the oceans are especially difficult to characterize because there are gaps in the fundamental knowledge about their climatology due in part to the absence of detailed, widespread observations (Haywood et al. 1999). Aerosols have a cooling effect on global climate, which can stabilize or perhaps even overcompensate the warming effect of greenhouse gases and thus lead to long-term cooling of the global climate (Schwartz 1996). Aerosol optical thickness (AOT) ranges from 0.02 over the open ocean to as high as 0.4 in industrialized and urban regions, and according to Wagener et al. (1997), an increase in the global average of 0.04 is sufficient to offset any longwave forcing from greenhouse gases.

Uncertainties in the contribution of aerosol loading is one of the largest sources of variability (error) in global climate models. Aerosols spanning in size from 10^{-4} to 10^{2} μm play an important role in air pollution and atmospheric solar radiation. Terrestrial aerosols (pollens, spores, and dust) and anthropogenic aerosols (biomass burning, sulfate transformation) spread over the world's oceans, where they may undergo wet or dry deposition, become dispersed, or be chemically transformed. Additional sources of aerosols are those naturally produced over the ocean, principally bursting bubbles and dimethylsulfide released by organisms. The concentration and size distribution of aerosols over the ocean is intimately linked to the synoptic-scale meteorological conditions that dictate air parcel trajectories. It is not uncommon to find large gradients in marine aerosol structure over relatively short distance scales (a few kilometers) or to find large areas with relatively uniform structure (1000 km^2).

An understanding of the aerosol optical thickness is essential in satellite remote sensing over the oceans because it relates directly to the amount of radiance received at the spacecraft. Satellite observations of ocean color yield the distribution of phytoplankton pigment concentration and production and thus provide global coverage of biogeochemical (carbon and nutrient) activity. A great deal of the uncertainty in satellite retrievals of pigment concentration comes from our inability to correct for aerosol scattering and attenuation of water-leaving radiance, and this is a subject of intensive research at this time. Typically, 90% of the top-of-atmosphere (TOA) irradiance is composed of photons that have not interacted with the water body (Viollier et al. 1980; Schwindling et al. 1998).

Corresponding author address: R. Michael Reynolds, Brookhaven National Laboratory, Environmental Sciences Department, Bldg 490d, Upton, NY 11973.
E-mail: reynolds@bnl.gov

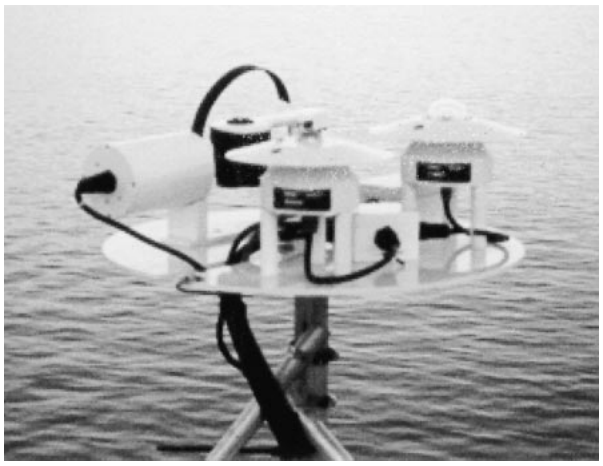

FIG. 1. Photo of the BNL portable radiation package (PRP). From left to right are the shadowband motor and FRSR head (wrapped in black insulation), the long-wave precision infrared radiometer (PIR), preamp, and shortwave PSP. The control-data unit and uninterruptable power supply are attached on the same vertical pole just beneath the plate.

This paper describes a fast-rotating shadowband radiometer (FRSR), a multispectral sun photometer that can be used to measure aerosol radiative characteristics from ships over the world's oceans. These measurements can be used to develop climatologies of the aerosol optical thickness and a direct link between the aerosol distribution and the climatic impact of the aerosols as well as to validate the atmospheric correction algorithms used in ocean color satellites. At present, aerosol optical thickness measurements can be made at sea using hand-held sun photometers or motion-stabilized sun photometers. Hand-held sun photometers are relatively accurate if several units are used together to make measurements but require operators and typically are not used to make continuous measurements. Motion-stabilized sun photometers are expensive and sophisticated and are not available for autonomous deployment. A shipboard shadowband radiometer, with gimbals and stabilization motors, was tested by Guzzi et al. (1985) but never developed into an operational instrument. The FRSR, described in this paper (Fig. 1), does not require an operator or motion stabilization and is a candidate for widespread deployment to produce climatologies of aerosol optical thickness. In addition, it measures the diffuse and global irradiance, which can be used for cloud and radiation studies as described by Long (1996), Long et al. (1996), and Long and Ackerman (1999, manuscript submitted to *J. Geophys. Res.*).

After a brief review of the theory of aerosol thickness in section 2, a complete description of the FRSR hardware is given in section 3. The sweep-by-sweep data analysis procedure is described in section 4. Field measurements and a calibration at Mauna Loa Observatory (MLO) are reviewed in section 5. Finally, in section 6, we discuss the implications of these measurements, recent new datasets, and plans for further improvements.

2. Background

a. Basic concepts

A sun photometer measures the directional solar irradiance in discrete wavelength channels along a vector from the instrument detector to the solar disk. The atmosphere both absorbs and scatters light along this vector, and these effects are treated together through the mass extinction cross section, k_λ (Liou 1980). Within narrow spectral regions, the different scattering and absorbing processes may be assumed to be independent of each other, and the total extinction coefficient is a simple sum from all the contributors (Gueymard 1998):

$$k_\lambda = k_A + k_R + k_O + k_X, \tag{1}$$

where the terms on the right represent the mass extinction cross sections for aerosol scattering, Rayleigh scattering, ozone (O_3) absorption, and all other absorbers taken as a group.

The other absorbers here include stratospheric and tropospheric nitrogen dioxide (NO_2), uniformly mixed gases, and water vapor. These absorbers can be considered to be secondary to the aerosols, ozone, and Rayleigh terms. The NO_2 absorption is most pronounced in the ultraviolet end of the spectrum (Davidson et al. 1988), and water vapor is strongest at the infrared end and beyond. Therefore, because this paper is focused on the technique of measurement and not on the details of the absorption chemistry, we will combine all other extinction terms with the aerosol scattering term (k_A).

A parallel beam of radiation, denoted by its irradiance, I_λ, will be reduced in the direction of its propagation by an amount given by

$$dI_\lambda = -k_\lambda \rho I_\lambda ds, \tag{2}$$

where k_λ is defined by (1), ρ is the air density, and ds is the differential pathlength. If k_λ is constant, the classical Beer–Bouguer–Lambert law results:

$$I_\lambda(s_2) = I_\lambda(s_1)e^{-k_\lambda u}, \tag{3}$$

where $u = \int \rho\, ds$ is called the optical thickness or optical path, and integration proceeds along the path the ray takes from s_1 to s_2.

In the atmosphere k_λ and ρ are not homogeneous, and so the full integration of (2) is required. A reasonable approximation is that the atmosphere is horizontally stratified, and this allows integration of (2) along the vertical axis, z, in a coordinate system on the earth's surface. Then $ds = \sec\theta dz$ and

$$I_\lambda(h) = I_{\lambda T} \exp\left(-\int_h^\infty k_\lambda \rho \sec\theta\, dz\right), \tag{4}$$

where $I_\lambda(h)$ is the irradiance at the observer at height h above sea level, and $I_{\lambda T}$ is the irradiance at the TOA. Integration follows the ray in its refracted path through the atmosphere and, for completeness, must include the curvature of the earth.

In the case that k_λ is constant through the air column, as in Rayleigh scattering, it can be moved outside the integral. In the cases when it is nonuniform in the column, as for aerosol and ozone, an effective extinction coefficient can be defined. The resulting effective total extinction coefficient is given by $\tilde{k}_\lambda = \tilde{k}_A + k_R + \tilde{k}_O$ and is defined by

$$\int_h^\infty k_\lambda \rho \sec\theta \, dz = \tilde{k}_\lambda \int_h^\infty \rho \sec\theta \, dz = \tau_\lambda \left[\frac{\int \rho \sec\theta \, dz}{\int \rho \, dz} \right]. \tag{5}$$

The terms with tildes are effective mean values that produce the same extinction if uniformly distributed through the atmosphere. The bracketed fraction is defined as the air mass, $m(\theta)$, and is a function of the zenith angle, θ. When the solar beam is normal to the geoid, $m = 1$, the normal AOT is defined as

$$\tau_\lambda = \int_h^\infty k_\lambda \rho \, dz = \tilde{k}_\lambda \int_h^\infty \rho \, dz. \tag{6}$$

The resulting formulation for the irradiance becomes

$$I_\lambda(h) = I_{\lambda T} e^{-(\tau_A + \tau_R + \tau_O) m(\theta)}, \tag{7}$$

which is a working analog to the classical Beer–Bouguer–Lambert equation, (3). Without knowing the vertical and horizontal distribution of the different contributing attenuators, (7) serves as a definition of the optical thicknesses that must be derived by observation of the extinction of the solar beam through the atmosphere.

The instantaneous solar irradiance at the top of the atmosphere, $I_{\lambda T}$, is the solar constant modulated by the earth–sun distance, $I_{\lambda T} = I_{\lambda 0}/r^2$, where $I_{\lambda 0}$ is the mean solar irradiance at the top of the atmosphere and r is the ratio of the earth–sun distance to its mean value (Paltridge and Platt 1977):

$$r = 1 - \epsilon \cos(a[J - 4]), \tag{8}$$

where $\epsilon = 0.016\,73$ is the eccentricity of orbit, $a = 2\pi/365.3 = 0.017\,201$, and J is the day of the year (sometimes referred to as the Julian day). The r^2 correction results in an annual modulation of $I_{\lambda 0}$ of approximately 6%. This is comparable to the uncertainty of about 5% in the measured solar spectrum (see Colina et al. 1996) (Fig. 2).

The air mass, also called atmospheric mass, $m(\theta)$, is a function of the path of the ray through the atmosphere. When refraction and the earth's curvature are ignored, the simple equation $m = \sec\theta_T$, where θ_T is the solar zenith angle at the top of the atmosphere, can be used. This approximation is accurate to within 1% when $\theta_T \leq 70°$. Kasten and Young (1989) include both curvature and refraction in a formulation of air mass and use the

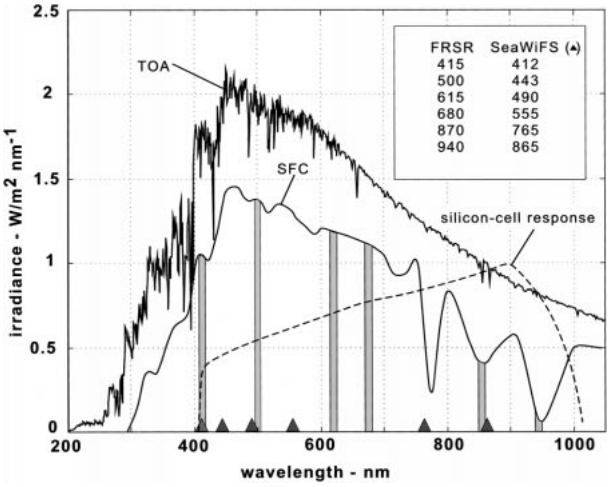

FIG. 2. Reference spectrum of solar radiance at the top of the atmosphere, the jagged line (Colina et al. 1996), and a typical spectrum at ground level, the smooth solid line. The shaded bars show the FRSR passbands for channels 2–7. Channel 1 is a broadband silicone call, and its response is shown by the dashed-line curve with peak value of 1 at approximately 900 nm. The current SeaWiFS satellite measures ocean color in six 20-nm bands, which are shown by the dark triangles.

ISO standard atmosphere for density and index of refraction. They use an index of refraction profile at 700 nm for all wavelengths and then fit the computations to an empirical curve,

$$m(\theta_r) \approx \frac{1}{\cos\theta_r + a(b - \theta_r)^{-c}}, \tag{9}$$

where θ_r is the solar zenith angle *relative to the observer* in radians, $a = 0.505\,72$, $b = 96.079\,95$, and $c = 1.364$. A pointing sun photometer locates the solar beam and thus automatically measures θ_r, but a shadowband instrument must compute it. The ephemeris algorithm by Michalsky (1988; Spencer 1989) is used to determine θ_r and θ_T given the time and geographic position of the observer and including refraction and curvature.

In (7), the last two normal optical thickness terms can be determined by a combination of measurements and theory. Rayleigh scattering is well understood, and τ_R can be computed by theoretical formulation. Tables of Rayleigh scattering coefficient, using the relationships from Penndorf (1957), were computed for each channel wavelength and for the atmospheric pressure at the time of the measurement with an empirical equation:

$$\tau_R = \left(\frac{p}{p_0}\right)(a_1\lambda^4 + a_2\lambda^2 + a_3 + a_4\lambda^{-2})^{-1}, \tag{10}$$

where $(a_1, a_2, a_3, a_4) = (117.2594, -1.3215, 0.000\,320\,73, -0.000\,076\,842)$, p is the atmospheric pressure (in hPa) at the time of the measurement, $p_0 = 1013.25$ hPa, and λ is the wavelength (in μm).

The ozone optical thickness can be computed from measurements of the ozone distribution or inferred from

known ozone climatology. The ozone corrections used in this paper are quite small and were provided by the National Aeronautics and Space Administration (NASA) (M. Wang 1999, personal communication).

b. Calibration considerations

Photometric instruments measure light through a bandpass filter and so all wavelength dependency must be integrated over the filter bandpass. Each detector has a different response function, $w_i(\lambda)$, where i is the detector (channel) number. Each detector-filter response is calibrated relative to its maximum value at its center wavelength, λ_i, and $w_i(\lambda_i) \equiv 1$. Its values at other wavelengths are referenced to its response at λ_i. The measured irradiance is related to the actual incident irradiance by the integral

$$I_i = \frac{\int_0^\infty w_i(\lambda) I_\lambda \, d\lambda}{\int_0^\infty w_i(\lambda) \, d\lambda}, \tag{11}$$

and all references to irradiance, as measured by an instrument, imply the above weighted mean based on a known bandpass filter response. The bandwidth of the filter is defined as the width of a top-hat unity-response function with the same area as the actual response

$$\Delta\lambda_i = \int_0^\infty w_i(\lambda) \, d\lambda. \tag{12}$$

In all discussions after this point, the λ subscript will be dropped unless it is necessary for clarity. All development refers to monochromatic light, and wavelength dependency is implicit. The instrument bandpass and its effect on a spectrum of light are also hereafter implied. The discussion below is applied to all channels in the same fashion, and so unless it is necessary for clarity, the i subscript will be omitted.

Taking the natural log of both sides of (7) results in the classic Langley relationship:

$$\ln(I_N) = -\tau m + \ln(I_T), \tag{13}$$

where $\tau = (\tau_A + \tau_R + \tau_O)$, and I_N is the measured irradiance of the solar beam referenced to a plane that is normal to the solar beam and excludes all scattered diffuse light. In the Langley method (Shaw 1983; Harrison and Michalsky 1994), a plot of m versus $\ln(I_N)$ can be extrapolated to $m = 0$ to derive $\ln(I_T)$. The negative of the slope of the line is τ. The Langley method works whenever the skies are perfectly clear, with no cirrus or other layers present, and if τ is constant over the time duration of the observations. In practice, a Langley plot can be produced from about 1 h of clear sky in the early morning just after sunrise or in the late evening just before sunset when $2 < m < 6$ ($60 < \theta_r < 80°$). All measurements of I_N are plotted on a log-linear plot, and a best estimate straight line is fitted to the data. For sites other than ideal calibration locations, such as the Mauna Loa Observatory described below, a median-fitting algorithm provides the best objective fit to the data. Over the ocean, there are almost always clouds on the horizon. In the Tropics these are usually high cumulus or cirrus clouds. As a result, Langley plots from ships are rare gems that must be collected whenever they occur.

Langley plots are constructed as often as possible as a quality assurance tool because they provide an excellent means of detecting calibration changes. The measured TOA irradiance, I_T, depends on the sun–earth separation, but its corrected value, $I_0 = I_T r^2$, should not change significantly over time. The absolute calibration of the instrument can be compared to the mean reference solar irradiance at the top of the atmosphere, I_{REF}, (Colina et al. 1996) by integrating the reference solar spectrum over the bandpass of the sensor [see Eq (11)] to obtain

$$I_{0\text{REF}} = \frac{\int_0^\infty w(\lambda) I_{\text{REF}}(\lambda) \, d\lambda}{\int_0^\infty w(\lambda) \, d\lambda}. \tag{14}$$

In a well-calibrated absolute instrument, $I_0 \approx I_{0\text{REF}}$. However, as long as the calibration constant I_0 is constant, as determined from multiple Langley plots, accurate AOT estimates are possible. While many investigators use raw voltages to calibrate their instruments, the extra step of computing I_0 is important, since it defines the radiative impact of the aerosol at the surface.

Once I_0 is established for an instrument, (13) is used to estimate aerosol optical thickness for each instantaneous measurement of I_N. From the time and geographic location of the measurement, I_T can be computed from the calibration constant, $I_T = I_0/r^2$, and m can be computed accurately from (9) or estimated by $\sec\theta_T$. After the contributions by Rayleigh scattering and ozone absorption are accounted for, τ_A remains.

c. Theory of shadowband radiometers

An estimate of τ can be made for every measurement of the solar beam irradiance I_N when there are no clouds in front of the solar disk. Two sun photometer designs are commonly used: a narrowbeam detector mechanically pointed in the direction of the sun or a wide-field-of-view radiometer with a solar occulting apparatus. The first type of sun photometer (see Holben et al. 1998) requires careful angular positioning but can provide additional information on forward scattering phase functions and thus help characterize the aerosol constituents. The latter type of radiometer, a shadowband radiometer, measures the diffuse and global (upper hemispheric) irradiance and computes I_N as the difference between

the two. The device gets its name from the hemispherical metal strip that rotates around the detector and blocks the direct solar beam to yield a signal that is from the sky only (after the effect of the arm is included).

One of the first rotating shadowband devices was a broadband device introduced by Wesely (1982). A more advanced broadband instrument using a thermopile-type broadband pyranometer has been developed by Long et al. (1996). The multifrequency rotating shadowband radiometer (MFRSR), developed by Harrison et al. (1994), uses independent interference-filter-photodiode detectors and an automated rotating shadowband technique to make spatially resolved measurements at seven wavelength passbands. The MFRSR achieves an accuracy in direct-normal spectral irradiance comparable with that of narrowbeam tracking devices. A significant advantage of the shadowband technique is that the global and diffuse irradiance measurements can be used to study overall radiative budgets (Long 1996). Our FRSR makes use of the MFRSR detector head.

The shadowband radiometer must properly measure the global and diffuse irradiances from which the direct-beam irradiance is derived by the subtraction

$$I_H = I_G - I_D, \tag{15}$$

where I_H is the direct-beam irradiance projected onto a horizontal plane, I_G is the global irradiance on the horizontal plane, and I_D is the diffuse irradiance from nonforward scattering. The global irradiance, I_G, is measured when the band is out of the field of view and the sensor is exposed to full sunlight. The irradiance normal to the incident beam is computed by

$$I_N = I_H \sec\theta_r. \tag{16}$$

A correction for the amount of sky that is blocked by the occulting band is essential for an accurate measurement. An automatic correction for the shadowband is possible through measurement of ''edge'' irradiance, as is done with the land-based MFRSR. The shadow irradiance I_S occurs when the sun is completely covered by the shadowband, but a portion of the diffuse irradiance is also blocked. The edge irradiance I_E is measured when the band is just to one side of the solar disk and provides a good estimate of the global irradiance minus the portion of sky that is blocked by the shadowband at the time it blocks the solar disk. In practice, I_E is selected from two measurements taken when the shadow is on one side or the other of the diffuser. Generally, an average is taken, but in some cases, in the early morning or late evening, only one of the edges is acceptable. It is easy to show that the fully corrected horizontal beam irradiance is

$$I_H = I_E - I_S. \tag{17}$$

An advantage of using (17) is that with the fast-rotating technique, the edge and shadow measurements are made in a very short time, which significantly reduces noise, especially on partly cloudy days. The electronic transfer function is linear with very small offset, and the bias is removed by subtraction.

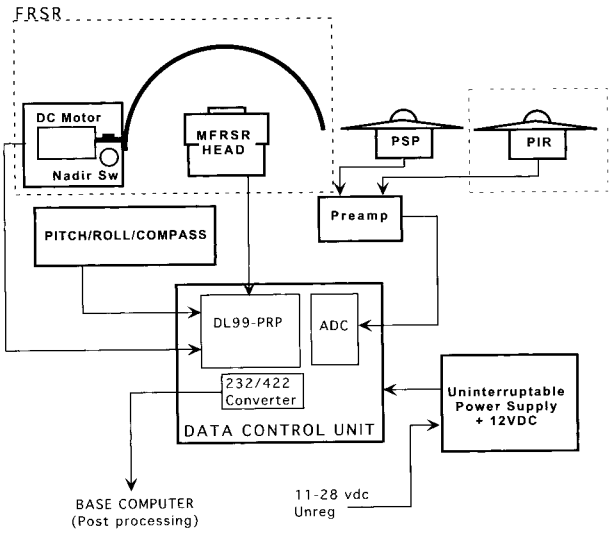

FIG. 3. Block diagram of the main components of the PRP. The FRSR provides spectral irradiance decomposition while the broadband instruments provide total shortwave and longwave flux measurements. The PIR is a broadband longwave instrument that has been added to later versions of the PRP.

3. Instrument details

a. Hardware description

The complete radiation package, shown in Fig. 1, is an integration of five primary components (Fig. 3): 1) a broadband pyranometer, model PSP from The Eppley Laboratory, Inc.; 2) the FRSR, which is the subject of this paper; 3) an attitude sensor that measures platform pitch, roll, and azimuth; 4) a small, low-power data-control unit that performs the sweep-by-sweep processing algorithms; and 5) an uninterruptable power supply and backup battery module that eliminates power surges, minimizes power supply noise, and supports wind or solar power operation for remote operation. This paper concentrates on the operation of the FRSR and the specialized data processing that is required to derive accurate spectral decomposition of solar insolation.

The FRSR shadowband rotates continuously and moves across the upper hemisphere in 3.4 s. The hemispherical shape of the shadowband ensures that the sensor will see a shadow, regardless of its azimuth heading and at all but minimal solar elevations. Typically, the shadow moves across the face of the sun in a few tenths of a second, and the head is in full shadow for about one-tenth of a second.

The multispectral FRSR head is manufactured by Yankee Environmental Systems, Inc. It is a modified version of the comercially available MFRSR spectral radiometer head and has seven detectors (channels): a broadband channel and six 10-nm-wide bandpass-fil-

tered channels at 415, 500, 660, 860, 870, and 940 nm. The head construction, adeptly described by Harrison et al. (1994), is environmentally sound, robust, and suitable for use in a marine environment. Figure 2 shows the Colina et al. (1996) reference solar spectrum at the top of the atmosphere and a typical spectrum for the earth's surface. Superimposed on the graph are the FRSR pass bands, the silicone cell photodiode (called broadband here), and the six narrowband spectral channels. Passbands on the SeaWiFS satellite are shown for comparison.

The FRSR head is modified to decrease its electrical response time to about 1 ms. The response of the silicone cell detector is well below 1 ms, but the internal preamplifiers in the stock head have integrating low-noise amplifiers, that slow the overall response. The head response times are decreased by reducing their low-pass filter capacitors. This is accomplished easily, and laboratory tests do not show additional noise in the measurements.

b. Laboratory calibrations

Calibration is the most essential element of a radiation measurement program. Climate studies require insolation averages to a few watts per meters squared in absolute accuracy, and photometric studies require zero drift in the end-to-end calibration constants for reliable estimates of optical thickness. A thorough and on-going calibration process is required before the FRSR can make accurate photometric measurements at sea.

Laboratory calibration is done in two parts: the electronics and the optical head. The end-to-end electronic gains are carefully calibrated using the data collection software and a precision millivolt reference source in place of each radiometer channel. One-minute averages and standard deviations of voltages for each channel are logged for a full range of input voltages. The output voltage range is approximately 0–3000 mV and standard deviations are typically <1 mV over the entire range. Electronic calibrations are repeated at regular intervals and for a variety of ambient temperatures. Calibration of the electronics is performed before and after each deployment, and the gain equations are constant.

The FRSR radiometer head comes fully calibrated by the manufacturer in the form of three tables. First is a linear, direct-normal irradiance gain equation with units of mV $(\text{W m}^{-2})^{-1}$ for the broadband channel and mV $(\text{W m}^{-2}\ \text{nm}^{-1})^{-1}$ for the narrowband channels. These calibration equations are corrected for the individual bandpass spectral responses for the head. The second calibration product is the bandpass spectral response for each narrowband channel. This is the $w_i(\lambda)$ function in Eq. (11). Each of the narrowband filters has a bandwidth of approximately 10 nm, and the calibration provides gain figures at 1-nm spacing. Finally, zenith angle correction is measured on two planes, one on a south-to-north plane and one on a west-to-east plane. The zenith angle corrections are determined by holding the head in a tilting fixture under a collimated beam and tilting the head through 180° in 1° steps from horizon to horizon in each plane. Calibration tilt angles are $\theta_{\text{SN}j}$ and $\theta_{\text{WE}j}$ for $j = 1, 2, \ldots, 181$. As an example, $\theta_{\text{SN1}} = 90°$ in the south direction, $\theta_{\text{WE136}} = 45°$ in the east direction, and so forth. A plot of the calibration zenith error corrections for the S–N and W–E planes are shown as a function of atmospheric mass in Fig. 4.

The electronic gains are combined with the direct-normal head irradiance gains coefficients to make a single calibration equation relating direct-normal irradiance to the electronic measurement in millivolts:

$$I_h = c_1 v + c_2, \tag{18}$$

where I_h is the irradiance, which is computed from the measured voltage v, and (c_1, c_2) are the calibration constants. In the case of a parallel beam of radiation, the measured irradiance flux into a plane that is parallel to the head surface is given by

$$I_h = \chi(\alpha_h, \theta_h) \cos\theta_h \int_0^\infty I_\lambda w_\lambda \, d\lambda \Big/ \int_0^\infty w_\lambda \, d\lambda, \tag{19}$$

where χ is the cosine correction calibration; α_h and θ_h are the beam azimuth and elevation angle, respectively, relative to the plane of the head; I_λ is the beam irradiance spectrum in a plane normal to the beam vector; and w_λ is the filter bandpass discussed above.

By combining (18) with (7), the measured voltage for a solar beam becomes

$$v_N = v_T e^{-\tau m} - \frac{c_2}{c_1}(1 - e^{-\tau m}), \tag{20}$$

and as long as the response is linear and the bias term is negligible (i.e., $|c_2/c_1| \ll 1$), one can use the voltage output to measure τ. A silicone cell photodiode has a small leakage current called a ''dark current.'' After amplification in the electronics, a dark voltage results, and if the dark voltage, $-(c_2/c_1)$, is not negligible, it must be measured and removed. Electronic bias is a consideration in interpreting Langley calibrations. In some instruments, such as the MicroTops handheld sun photometer (Solar Light Company 1996), the operator covers the detector before taking a solar measurement. For an autonomous instrument, it is better to choose an electronic design that eliminates the dark voltage. For the FRSR, the largest deviation from a straight line fit is 0.2 W m^{-2} for the broadband channel and 0.002 W $\text{m}^{-2}\ \text{nm}^{-1}$ for the narrowband channels, which is less than 0.1% of full scale.

Calibration drift in the multifrequency head has caused a great deal of consternation to the sun photometer community. Calibration shift is detectable as a permanent change in I_0 (or its voltage analog v_0) as computed by the Langley method. Calibration shift is erratic and quite variable; it can occur suddenly, over a few weeks, or can degrade slowly over months. The 610-

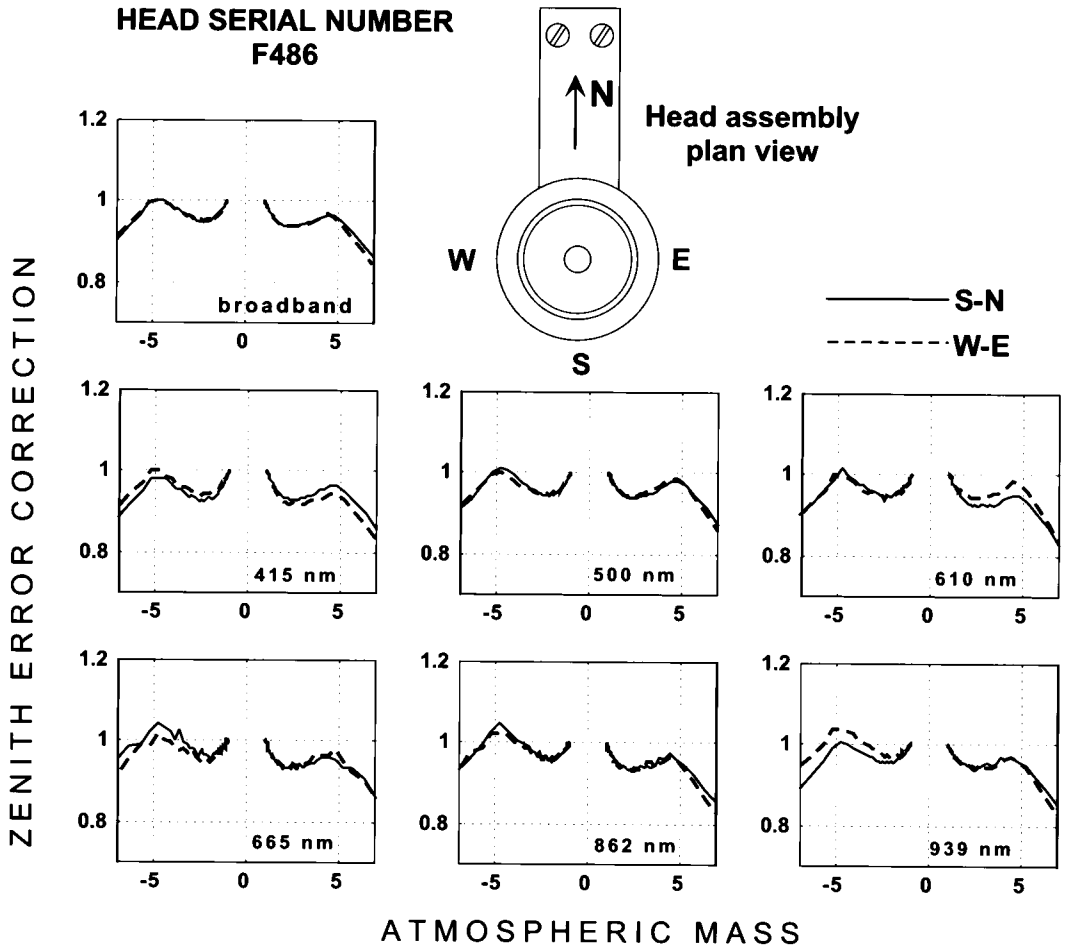

FIG. 4. The correction term for zenith angle cosine response for each channel of FRSR head number F486 plotted against atmospheric mass. The correction is measured by rotating the sensor in orthogonal directions, E–W and N–S. The two curves track closely but diverge somewhat (0.5%) at angles greater than 60° ($m > 2$). The differences between the curves relate to the position of each silicone detector in the head.

and 660-nm channels are most prone to drift, though all narrowband channels are suspect. Researchers suspect that the gain drift is due to a shifting bandpass response. In earlier heads, the filter material, a stack of laminated films, apparently became delaminated as a result of temperature cycling and humidity. A different filter material became available after approximately December 1998 (Barr Associates; see their Web site: barrassociates.com/terms/temperature.html), and many researchers are in the process of retrofitting their heads with the new material. The filter material is also sensitive to temperature, and the shift in center frequency for any narrowband filter is approximately $10^{-5}\lambda_0\Delta T$. Thus, if the head temperature varies from 20° to 30°C, the 500-nm filter will drift by less than 1 nm (M. Beaubean, Yankee Environmental Systems, 1999, personal communication).

The MFRSR head is well insulated (thermal time constant $\approx$ 15 min) and has a 25-W heater circuit. A temperature regulation circuit easily maintained the head internal temperature at 35°C. An added benefit from heating is that condensation inside the head and on the diffuser is eliminated by the elevated temperature. The electronic amplifier circuits were carefully designed and tested from −20° to 65°C, and no significant temperature dependence was observed.

c. Installation and operation

The control data unit, shown in Fig. 3, is custom-made and packaged in a waterproof housing that resides in close proximity to the sensors. The complete datalogger package incorporates radio interference and surge protection, operates over a −40° to 65°C temperature range, and is waterproof and immune to shock and vibration. The low-level analog signals from the FRSR head are digitized with a high-speed 12-bit analog-to-digital converter circuit.

The installation location of the instrument on a ship must be carefully selected. Ideally, the FRSR should be mounted in an exposed location as high as possible and

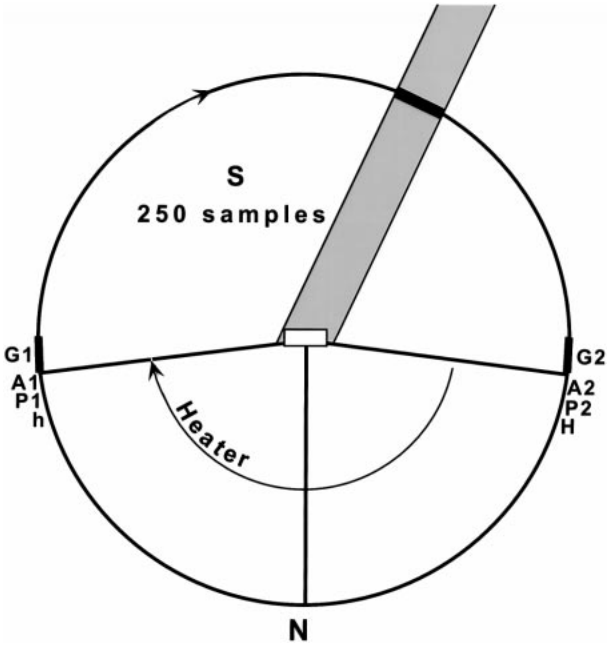

FIG. 5. The sequence of operations as the shade arm makes a cycle around the sensor. Timing begins when the shadowband crosses the nadir position (N). After approximately 0.2 of a cycle, the heater is turned off (h) to prevent any interference of the heater current in the detector electronics. After this, the pitch/roll/azimuth sensor is read (P) and the broadband signals measured (A). During the sweep (S), 250 samples are taken from each of the seven channels. After the sweep, the broadband and pitch/roll/azimuth are measured a second time and the heater is turned back on (H) if the head temperature is less than 35°C. The first and last 10 sweep samples are averaged for the global irradiance measurements, (G1) and (G2).

free of nuisance shadows from other objects. This is often difficult. Radiative flux measurements on a ship always need to consider errors from the ubiquitous masts and antennas. A ship's communication antennas have highest vertical priority, as do the running lights, and one must be careful of radar beams, which can cause severe electronic noise.

Several external observations are necessary for data analysis. Accurate time, latitude, and longitude are needed to compute solar zenith and azimuth angles. To correct the sensor's cosine response, one also needs the ship's pitch, roll, and heading so the exact angle between the normal of the head and the solar beam can be derived. A pitch-roll-compass sensor is read twice during each cycle of the shadowband. A GPS receiver provides time, position, and magnetic variation each second.

The control data unit performs several functions during each shadowband cycle (Fig. 5). Broadband and housekeeping measurements are taken when the arm is at each horizon. During the sweep, when the shadowband crosses the upper hemisphere, 250 measurements are made for each channel. The first and last 10 samples of each sweep are averaged, and we refer to these measurements as the global measurements, v_{G1} and v_{G2}. Global measurements are computed for each filter channel. To minimize electrical interference, the heater is operated only while the shadowband is below the horizon, and in cruises thus far, a constant head temperature of 35° ± 0.5°C is easily maintained.

At the end of each sweep of the shadowband, the channel-1 voltage measurements are examined, and a decision is made whether a viable shadow was present. The shadow ratio is a sensitive measure of the intensity of the direct solar beam and is computed by the equation

$$\kappa = \frac{v_{\text{av}} - v_{\text{min}}}{\sigma_v}, \tag{21}$$

where v_{av} is the mean signal voltage for the entire sweep, v_{min} is the minimum signal voltage, and σ_v is the standard deviation for the sweep. (Measurements at the time of the minimum signal ±0.3 s are excluded from the computation of mean and standard deviation.) After extensive field testing, an empirical criterion of $\kappa \geq 2.3$ has been found to capture almost all true shadow cases and seldom permits a false positive. A statistical argument for this value is as follows. In a completely overcast situation, the 250 sweep measurements could be considered to be independent samples with a Gaussian probability distribution, and there is approximately a 13% chance that any of the 250 samples would have a minimum that exceeded the 2.3 criterion. On sunny days, the shadow ratio can exceed a value of 200.

Any sweep with $\kappa \geq 2.3$ is block averaged and stored in a compressed binary packet. Block averaging of the sweep retains all of its significant shape characteristics but significantly reduces data storage requirements. Block averaging begins at the minimum index value, i_{min}, and moves left and right through the sweep array with increasing block sizes. Twenty-three contiguous block averages, b_{ij}, where i is the channel number 1–7 and j is the bin number, are computed according to Table 1. The shadow index, i_{min}, depends on the solar azimuth and zenith angles, the ship heading, and the pitch and roll, and thus can occur anywhere in the 250-point sweep array. In the block averaging process, some bins fall outside the sweep and are given a ''missing'' value.

The sweep data must be transmitted over long cables in noisy electronic environments, and therefore, standard packet conventions are used to ensure error-free

TABLE 1. Table of sweep block averaging bins, b_{ij}, $i = 1, \ldots, 23$; $j = 1, \ldots, 6$. The 23 bins and the number of points in each bin are shown. Bin 12 is the minimum (shadow) point.

1	2	3	4	5	6	7	8	9	10	11	12	13	14	15	16	17	18	19	20	21	22	23
30	20	20	10	10	10	5	5	5	5	5	1	5	5	5	5	5	10	10	10	20	20	30
											↑											

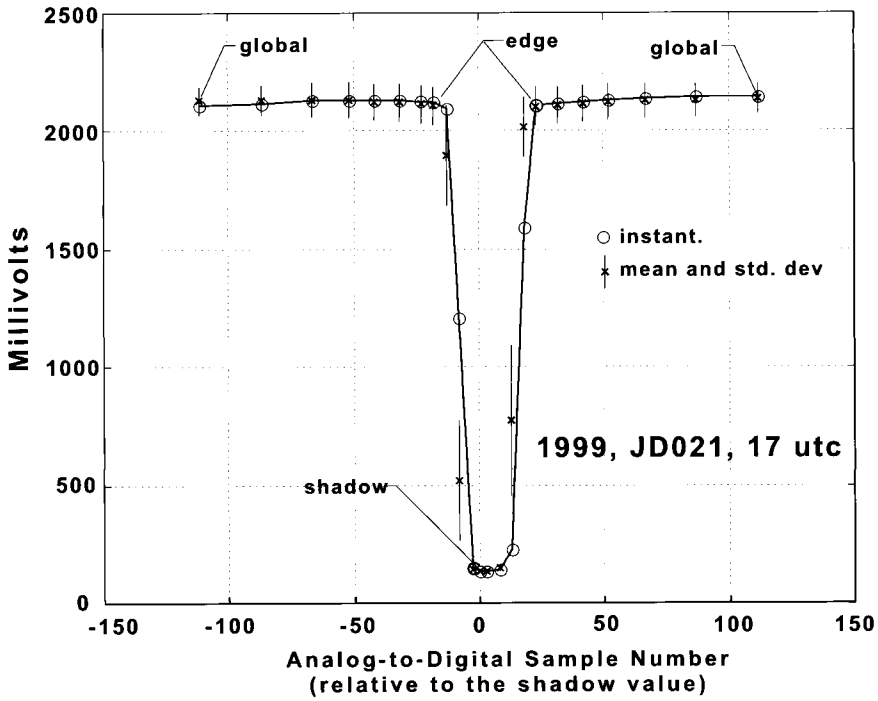

FIG. 6. An example of an instantaneous bin-averaged sweep (open circles) and a 2-min average of sweeps centered on the same time (crosses are the means and the standard deviations are vertical lines). The global, edge, and shadow values are marked.

communication. The compressed binary packet, with global and sweep data for all detectors, is transmitted as an EIA422, 19 200 bps, serial stream to the base computer. An EIA422 balanced-line transmission is highly immune to electronic noise and radio interference and can be transmitted over long transmission lines. The binary packet has start and end character strings and a cyclic redundancy checksum (CRC) for error-free transmission. Once the packets are transmitted, the shadowband cycle begins again.

4. Postprocessing

a. Sweep averaging

On a moving platform, some smoothing of the data is necessary. It was found that simple averages over a 2-min period (16 sweeps) would reduce the sampling uncertainty by a factor of approximately 4 and yield worst-case measurement uncertainties of about 5 W m^{-2} for the global values and less than 1 W m^{-2} for the shadow value. For perspective, 2 min is the approximate time for the sun to move by one diameter across the celestial sphere.

An example of the effectiveness of the 2-min averaging process is shown in Fig. 6, taken during the Aerosols99 cruise (discussed below). For this example the sun was high in the sky, and ship pitch and roll had a standard deviation of about 2°. (This amount of motion is typical for an 88-m ship in fair-weather ocean conditions.) When the detector was in full shadow, the standard deviations were extremely low and amounted to less than ± 1 W m^{-2}. During the time the detector was partially covered, the standard deviations were quite high due to the rapid transition and platform motion. When the detector was out of the shadow, standard deviations were small but were larger than the full-shadow case. Strict requirements are placed on the acceptability of any 2-min block. At least 14 sweeps must pass the shadow ratio criterion. Otherwise, that particular 2-min period is excluded from further analysis.

The diffuse component of total irradiance is insensitive to platform motion. Clouds alter the integrated diffuse irradiance on a timescale that is slow compared with the averaging times considered, as long as they do not block the direct beam. The minimal standard deviations in the shadow measurement in Fig. 6 are evidence to this fact.

The effectiveness of a 2-min averaging scheme was demonstrated by tests with an automated tilting table. During a cloud-free day, the tilting table was set to $\pm 5°$ in pitch and roll and to a rocking period of 6.7 s, and it was turned on and off in half-hourly intervals. Figure 7 compares the individual sweep measurements to the averages. The black curve shows mean global voltages from individual sweeps, and the white line is the result from the 2-min averaging process.

b. Decomposing the solar signal

The shadowband theory [outlined in Eqs. (15) and (16)] must be modified for a moving platform when the

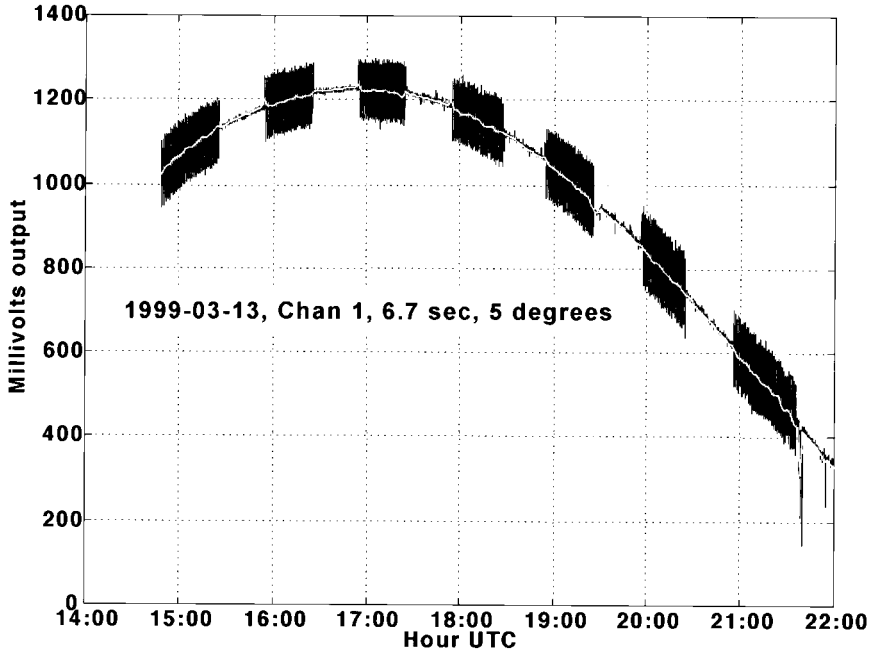

FIG. 7. A result from a tilting table experiment. The tilting table was set to 5° pitch and roll and 6.7-s period and operated each consecutive half hour. The black curve is data from each individual sweep and the white line is the result from the averaging process.

head might not be on a horizontal plane. Three measurement quantities for each channel are computed from the 2-min mean voltages: the global signal v'_G, the shadow signal v'_S, and the edge value v'_E. The primes indicate that the measurement is referenced to the plane of the head, which can be different than a horizontal plane. The two global measurements v_{G1} and v_{G2} are combined to produce the best estimate global voltage, v'_G. The mean shadow voltage is v'_S. The edge value is selected from the 2-min composite sweep using an objective algorithm that accounts for the fact that the width of the shadow depends on solar zenith and relative azimuth. The objective selection of the edge voltage uses one or a mean of both edge measurements to get the best estimate of v'_E.

The direct-beam irradiance falling onto the plane of the instrument is given by

$$v'_H = v'_E - v'_S. \tag{22}$$

This equation automatically corrects for the sky that is blocked by the shadowband and also removes any bias term in the calibration equation, (18). An important point in (22) is that the right-hand quantities are measured in a few tenths of a second, while the shadow crosses the diffuser. In such a short time interval, the ship attitude changes insignificantly, and interference from moving clouds is minimized.

The diffuse component of the solar signal is computed from

$$v_D = v'_G - v'_H, \tag{23}$$

and as we have stated previously, v_D is relatively unaffected by small amounts of platform motion.

The exact azimuth and elevation of the solar beam *relative to the head* must be computed from the following externally measured variables:

$$\{\alpha_h, \theta_h\} = f(\alpha_S, \phi_P, \phi_R, \alpha_r, \theta_r), \tag{24}$$

where $\{\alpha_h, \theta_h\}$ are the solar azimuth angle and solar zenith angle relative to the plane of the head, α_S is the mean heading of the ship in true coordinates, ϕ_P is the ship mean pitch, and ϕ_R is the corresponding mean roll over the 2-min period. The relative solar azimuth and zenith angles in geographic coordinates, as seen by the observer, are α_r and θ_r. Relationship (24) uses three two-dimensional coordinate transformations in heading, pitch, and roll to shift the solar beam vector from an earth-based coordinate system to a coordinate system aligned with the FRSR head. The matrix transformation technique is well known and discussed in many textbooks on matrix algebra. Once α_h and θ_h are known, the calibration table can be consulted, and an interpolated correction value, $\chi(\alpha_h, \theta_h)$, can be derived.

The direct-beam irradiance on a horizontal plane relative to the instrument, v'_H, is converted to a direct-beam irradiance into a plane normal to the solar beam using the relationship

$$v_N = \frac{v'_H}{\chi(\alpha_h, \theta_h)\cos\theta_h}. \tag{25}$$

The global and horizontal voltages are recomputed for the earth frame of reference:

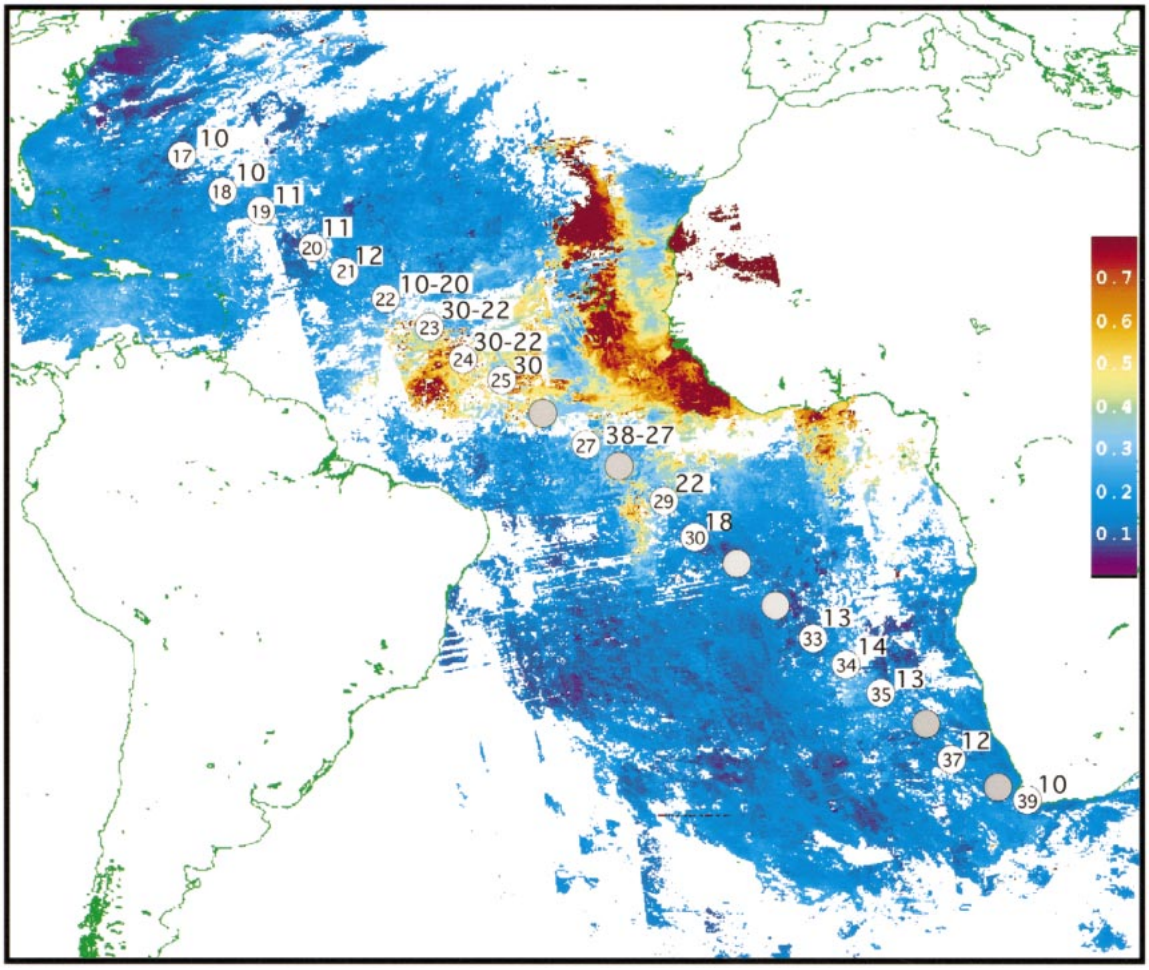

FIG. 8. The cruisetrack of the R/V *Ronald H. Brown* across the Atlantic on the first leg of the Aerosols99 cruise. The color key represents satellite-derived AOT. The white circles show the position of the ship at solar noon, and the year–days are shown in the circles. The approximate noon values of $\tau_A \times 100$ for the 610-nm band are shown adjacent to the circles. The trackline and AOT measurements are superimposed over a composite image of AOT at 630 nm. The composite was derived from direct downlink, 1-km resolution data from the *NOAA-14* AVHRR. The AOTs were derived only after the data passed a restrictive cloud-filtering algorithm and after manual editing. All received, cloud-free pixels were averaged in 1-km areas, and thus the image represents the AOT field at the time the ship was within 1000–2000 km of the pixel. The figure was provided courtesy of Phil Durkee and Kurt Nilsen of the Naval Postgraduate School and James Johnson of NOAA–PMEL.

$$v_H = v_N \cos\theta_r, \quad \text{and} \quad v_G = v_H + v_D. \tag{26}$$

The calibration equation, (18), is used to compute I_G, I_D, I_H, and I_N from v_G, v_D, v_H, and v_N, respectively. From these terms, Eq. (13) can be used either for estimating the calibration constant I_0 or for estimating τ_A.

5. Field deployments and Langley calibrations

Over the past three years, different models of the FRSR have been deployed on five ocean cruises. Early cruises allowed us an opportunity to watch system performance and make improvements to hardware and software as a continuing process. On 14 January 1999, the FRSR began a long voyage on the National Oceanic and Atmospheric Administration (NOAA) ship R/V *Ronald H. Brown,* first from Norfolk, Virginia, to Cape Town, South Africa, and then to Mauritius and on to the Indian Ocean for the INDOEX cruise (Parsons and Dickerson 1999). Figure 8 shows the track of the cruise as the ship sailed across the Tropics then through the south Atlantic Ocean to Cape Town. The cruise trackline is marked by circles that show where the ship was at 1200 UTC each day. Gray circles indicate very cloudy days when no AOT data were available. The numbers adjacent to each circle mark the AOT at 610 nm that was estimated by the FRSR, and these can be compared to the contours. The trackline is superimposed on a composite of Advanced Very High Resolution Radiometer (AVHRR) derived AOT at 630 nm for the cruise time period. The composite shows that over the course of the cruise, the ship encountered clean north Atlantic air followed by what appears to be Saharan dust then biomass

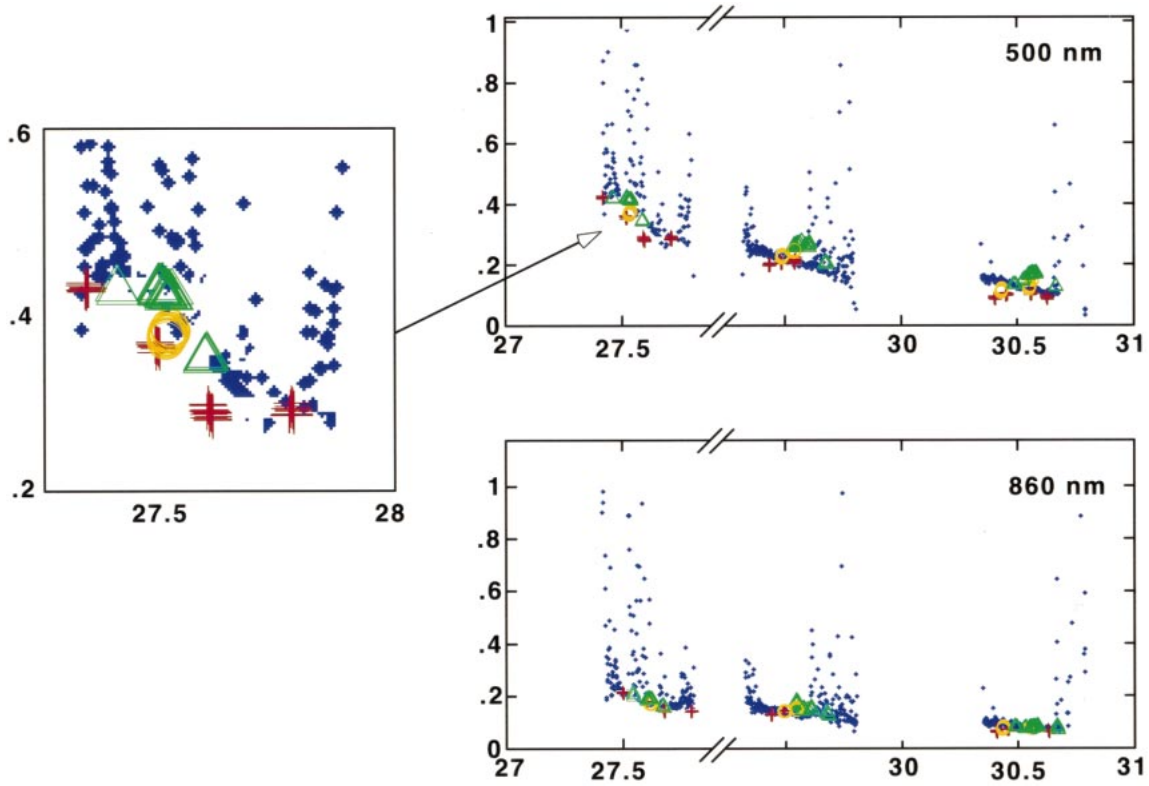

FIG. 9. AOT measurements during days 027, 029, and 030 during the Aerosols99 cruise to Cape Town. Day 028 was cloudy. Data for 500 and 862 nm are shown here because these are the same as the corresponding MicroTops bands. The FRSR data points (small blue crosses) are computed from each 2-min measurement, and the clear-beam, uncontaminated AOT measurements are discernable by the envelope denoting the minimum values. During this time the ship was leaving the contaminated African plume and entering the clean south Atlantic air. Day 28 was cloudy all day and no data were taken. The MicroTops measurements for PMEL (triangles), ARL (circles), and BNL (crosses) are superimposed on the FRSR data points. There are obvious differences in the spectral shape during this period.

burning from the central African continent and on into very clean south Atlantic air.

Details of this fascinating dataset will appear in future articles from the Aerosols99 team, but days 27–30 are shown here to demonstrate the performance of the FRSR at sea. During this time (Fig. 9), the AOTs changed dramatically as the ship left the continental plume and entered the South Atlantic clear air. Seas during this period were typical for the cruise; wave heights were estimated as 1–2 m and winds were 5–10 m s^{-1}. The mean pitch and roll were of the order of 1°, and their standard deviations were 1°–2°. Figure 9 shows the AOTs at 500 and 862 nm that were measured during the day. When clouds of any kind block the solar disk, the AOT rises dramatically, and these extraneous points are also shown. The clear-beam AOT is readily apparent as an envelope marking the minimum of the computed AOTs. One can clearly see the decrease in AOT during this period. The strong decrease in the 500-nm AOTs compared to the 862-nm band is evidence that we were moving from denser, finer particles to the more uniform and larger sea-salt particles that dominate open ocean conditions.

Also shown on the AOT panels are measurements from three different handheld sun photometers. The MicroTops units were also calibrated after the cruise at Mauna Loa Observatory, and the data here incorporate the validated calibration coefficients. The three MicroTops photometers used for comparison here were from Brookhaven National Laboratory (BNL, crosses), NOAA Atmospheric Resources Laboratory (ARL, circles), and NOAA Pacific Marine Environmental Laboratory (PMEL, triangles). The details of the MicroTops performance, calibration, and instrument-to-instrument scatter will be discussed in a separate paper, and they are used here for comparison to the FRSR. In general, the PMEL MicroTops did not perform well at 500 nm. There is no explanation for this since the MLO calibration showed no problems in this channel. Aside from that issue, the FRSR and MicroTops performed comparably. The exodus from the African plume is quite readily apparent in the FRSR data and not as discernable from the MicroTops.

During this period, we were able to get two good Langley days. Day 033 had a clear evening, and a second good opportunity for a midcruise Langley calibra-

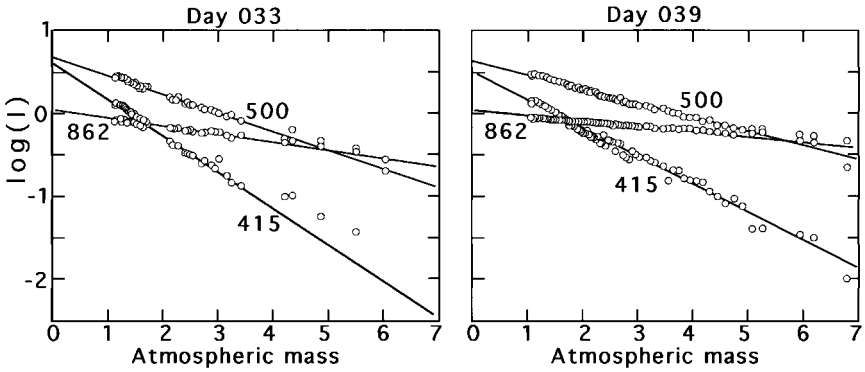

FIG. 10. Langley plots for days 033 and 039 during the Aerosols99 cruise. Channels at 415, 500, and 862 nm are shown. On day 033, mean tilt of the ship was approximately 1° and the 2-min standard deviation in tilt was 3°. The Langley conditions occurred in the evening. On day 039, the ship was in port in Cape Town, South Africa. The mean tilt was near zero, and Langley conditions occurred in the morning. The optical thicknesses τ represented by the slopes of the lines, were greater on day 033, but the extrapolated zero crossings I_T and the resulting calibration factors I_0 (see Table 2) are consistent.

tion check occurred on day 039 while the ship was tied to a pier in Cape Town. Langley plots for these three days are shown in Fig. 10. We had the most confidence in the channels at 415, 500, and 862 nm owing to filter drift problems discussed above, and these are shown in the plots.

After Cape Town, the FRSR was operated throughout the next four and a half months as the ship participated in experiments in the Indian Ocean. It was removed from its mast in Darwin in June, and in July 1999, it was taken to the NOAA Mauna Loa Observatory for calibration. Mauna Loa Observatory (Miller 1978) is at 3396 m altitude, well above the subtropical inversion, and removed from industrial sources of pollution or blown dust. Calibrations here are uncontaminated, and by taking measurements from a land-based site, platform motion is removed as a potential issue. Langley methods of calibration are sensitive to temporal variations of τ_A (Shaw 1983), and this is minimal at the isolated Mauna Loa site. The MLO is operated by the NOAA Climate Monitoring and Diagnostics Laboratory (CMDL), where a large suite of long-term baseline instrumentation is operated.

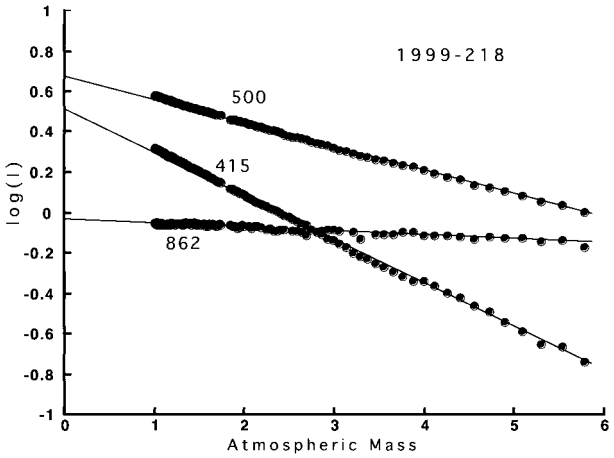

FIG. 11. A Langley plot for day 1999–219 from the Mauna Loa Observatory calibration. The clean dry air at the 3500-m altitude yields exceptionally low τ values, but the I_0 (see Table 2) are consistent with the earlier values.

Figure 11 shows results for day 219 (7 August 1999) during the Mauna Loa calibration. There is no question as to the quality of these conditions. In all Langley plots, the extrapolated intercepts, after being corrected for r^2, agree almost perfectly, and we can conclude that for these channels, the solar constant term I_0 was constant throughout the cruise.

As a cross-check on the accuracy of the factory calibrations, the measured values of I_0 from the Langley method were compared to the top-of-the-atmosphere absolute flux, as measured by satellites and precision ground measurements. An absolute flux calibrated reference spectrum of the sun covering the 120–2500-nm range to an accuracy of 5% (Colina et al. 1996) was used in this comparison. The spectrum was corrected for the sun–earth distance and convolved with the bandpass response from the head calibration as described in (14). Table 2 shows the results.

6. Conclusions

The fast rotating shadowband spectral radiometer (FRSR) was developed for making long-term, routine, downwelling radiation measurements from moving platforms, such as ships. The design, described in this paper, and results from the Aerosols99 cruise across the Atlantic Ocean demonstrate the effectiveness of the FRSR for shipboard sun photometric measurements in the world's oceans.

The diffuse irradiance $I_D(\lambda)$ is rarely measured at sea, and the ability to do this in an automated, routine manner

TABLE 2. Table of comparisons of I_0 from Langley plots from three different days. For the three filters shown, μ is the mean value, σ is the standard deviation relative to the reference value, and δ is the relative difference of the mean value from the weighted Colina et al. (1996) value.

		$I_0 = I_1 r^2$		
	r	415 nm	500 nm	862 nm
JD33	0.9854	1.791	1.914	1.020
JD39	0.9803	1.752	1.937	0.969
JD219	1.0141	1.752	2.028	1.015
I_{0REF}	1.0000	1.758	1.908	0.992
μ		1.765	1.959	1.0013
σ		1.3%	3.2%	2.8%
δ		0.4%	2.3%	1.1%

μ = mean (I_0); σ = [std dev(I_0/I_{0REF}]100%; δ = [($I_0 - I_{0REF}$)/I_{0REF}]100%.

will provide additional information on the composition of the measured aerosols. Diffuse irradiance and the ratio of the direct normal to diffuse irradiances are important climate parameters.

We have emphasized the importance of calibrations for FRSR measurements, which is the same as the land-based MFRSR and related instruments. A major difficulty for the oceanic instrument is that good ''Langley days'' occur so rarely at sea, owing to ubiquitous clouds on the horizon. A special effort to either identify those rare Langley days and also to maintain a schedule for instrument exchange and land calibration is essential. Oceanic conditions are generally much more clean and homogeneous than terrestrial sites. The Langley method makes an assumption of a stable and uniform atmosphere, and this is often questionable. With good calibration, one should be able to achieve 1% repeatability in I_0, and while we have not achieved this in the current work, we can see that such a figure is acheivable.

During the next year, we expect to produce considerable field data from this and other FRSR systems presently under construction. We will be adapting the software, currently research oriented, into a reliable autonomous package that is suitable for a volunteer ship program. Extensive testing of the instrument using a pitch–roll table on land sites, at-sea intercomparisons, and long-term shipboard datasets is expected to set bounds on the usefulness of the FRSR in different ocean settings and platforms.

Acknowledgments. This development was accomplished with support from the U.S. Department of Energy's Atmospheric Radiation Measurement Program (ARM) and the National Aeronautics and Space Administration Sensor Intercomparison and Merger for Biological Interdisciplinary Ocean Studies (SIMBIOS) program, Contract 52-210.91. The mechanical and electronic engineering were performed by Scott Smith and Ray Edwards of BNL. The officers and crew on the R/V *Ronald H. Brown* were completely supportive of our effort and went beyond expected duties to accommodate our installations. During the Aerosols99 cruise, we received considerable support and mentoring from scientists Tim Bates, Ken Voss, and Bruce Dodderidge. Chuck Long of Pennsylvania State University conceived the original idea for this modification to the classical shadowband instrument. Lee Harrison of SUNY–Albany provided helpful comments and suggestions. Tom Ackerman and Ted Cress of Pacific Northwest National Laboratory encouraged our work throughout. We also appreciate the efforts of Kendall Carder and Bob Stewart at the University of South Florida for helping us test the original prototype of this instrument aboard the R/V *Bellows.*

REFERENCES

Colina, L., R. C. Bohlin, and F. Castelli, 1996: The 0.12–2.5 μm absolute flux distribution of the sun for comparison with solar analog stars. *Astron. J.,* **112,** 307–315.

Davidson, J. A., C. A. Cantrell, A. H. McDaniel, R. E. Shetter, S. Madronich, and J. G. Calvert, 1988: Visible–ultraviolet absorption cross sections for NO_2 as a function of temperature. *J. Geophys. Res.,* **93** (D6), 7105–7112.

DOE, 1996: Science plan for the Atmospheric Radiation Measurement Program (ARM). Rep. DOE/ER-0670T, U.S. Department of Energy, Office of Energy Research, 50 pp.

Gueymard, C. A., 1998: Turbidity determination from broadband irradiance measurements: A detailed multicoefficient approach. *J. Appl. Meteor.,* **37,** 414–435.

Gurney, R. J., J. L. Foster, and C. L. Parkinson, 1993: *Atlas of Satellite Observations Related to Climate Change.* Cambridge University Press, 470 pp.

Guzzi, R., G. C. Maracci, R. Rizzi, and A. Siccardi, 1985: Spectroradiometer for ground-based atmospheric measurements related to remote sensing in the visible from a satellite. *Appl. Opt.,* **24,** 2859–2864.

Harrison, L., and J. Michalsky, 1994: Objective algorithms for the retrieval of optical depths from ground-based measurements. *Appl. Opt.,* **33,** 5126–5132.

——, ——, and J. Berndt, 1994: Automated multifilter rotating shadow-band radiometer: An instrument for optical depth and radiation measurements. *Appl. Opt.,* **33,** 5126–5132.

Haywood, J. M., V. Ramaswamy, and B. J. Soden, 1999: Tropospheric aerosol climate forcing in clear-sky satellite observations over the oceans. *Science,* **283,** 1299–1303.

Holben, B. N., and Coauthors, 1998: AERONET—A federated instrument network and data archive for aerosol characterization. *Remote Sens. Environ.,* **66,** 1–16.

Hooker, S. B., W. E. Esaias, G. C. Feldman, W. W. Gregg, and C. R. McLain, 1992: *An Overview of SeaWiFS and Ocean Color.* SeaWiFS Tech. Rep. Series, Vol. 1, Tech. Memo 104566, NASA, 24 pp.

Kasten, F., and A. T. Young, 1989: Revised optical air mass tables and approximation formula. *Appl. Opt.,* **28,** 4735–4738.

Kiehl, J. T., 1999: Solving the aerosol puzzle. *Science,* **283,** 1273–1275.

Liou, K.-N., 1980: *An Introduction to Atmospheric Radiation.* Academic Press, 392 pp.

Long, C. N., 1996: Surface radiative energy budget and cloud forcing: Results from TOGA COARE and techniques for identifying and calculating clear sky irradiance. Ph.D. thesis, The Pennsylvania State University, 193 pp.

——, C. F. Pavloski, and T. P. Ackerman, 1996: A rotating shadow arm broadband solar radiometer: Instrument design and concept verification using ARM SGP radiometer measurements. *Proc. Sixth Atmospheric Radiation Measurement Science Team Meet-*

ing, U.S. Department of Energy, Pacific Northwest National Laboratory, 200 pp.

Michalsky, J. J., 1988: The Astronomical Almanac's algorithm for approximate solar position (1950–2050). *Sol. Energy,* **41,** 227–235.

Miller, J., Ed., 1978: *Mauna Loa Observatory: A 20th Anniversary Report.* National Oceanic and Atmospheric Administration.

Paltridge, G. W., and C. M. R. Platt, 1977: Radiative processes in meteorology and climatology. *Developments in Atmospheric Science,* Elsevier.

Parsons, Capt. R. L., and R. R. Dickerson, 1999: NOAA Ship *Ronald H. Brown* study global climate variability. *Sea Technol.,* **June,** 39–45.

Penndorf, R., 1957: Tables of refractive index for standard air and the Rayleigh scattering coefficient for the spectral region between 0.2 and 20.0 μ and their application to atmospheric optics. *J. Opt. Soc. Amer.,* **47,** 176–182.

Schwartz, S. E., 1996: The Whitehouse effect—Shortwave radiative forcing of climate by anthropogenic aerosols: An overview. *J. Aerosol Sci.,* **27,** 359–382.

——, and M. O. Andreae, 1996: Uncertainty in climate change caused by aerosols. *Science,* **272,** 1121–1122.

Schwindling, M., P.-Y. Deschamps, and R. Frouin, 1998: Verification of aerosol models for satellite ocean color remote sensing. *J. Geophys. Res.,* **103** (C11), 24 919–24 935.

Shaw, G. E., 1983: Sun photometry. *Bull. Amer. Meteor. Soc.,* **64,** 4–10.

Solar Light Company, 1996: User's guide for the Microtops II Ozone and Sun Photometer. Rep. MTP03, Solar Light Co., 53 pp.

Spencer, J. W., 1989: Comments on The Astronomical Almanac's algorithm for approximate solar position (1950–2050). *Sol. Energy,* **42,** 353.

Viollier, M., D. Tanré, and P.-Y. Deschamps, 1980: An algorithm for remote sensing of water color from space. *Bound.-Layer Meteor.,* **18,** 247–267.

Wagener, R., S. Nemesure, and S. E. Schwartz, 1997: Aerosol optical depth over oceans: High space- and time-resolution retrieval and error budget from satellite radiometry. *J. Atmos. Oceanic Technol.,* **14,** 577–590.

Wesely, M. L., 1982: Simplified techniques to study components of solar radiation under haze and clouds. *J. Appl. Meteor.,* **21,** 373–383.